Supplementary Information

Atomic Ni-doped ZrO_2 with subnanometric Fe clusters for tandem C–C bond cleavage and coupling

Xin Zhao,[a] *Jie Wen,*[a] *Qian Qiang,*[b,c] *Dawang Tang,*[a] *Fengliang Wang,*[a] *Ruiqi Fang,**[a] *Changzhi Li,*[b,c] *and Yingwei Li,**[a]

[a] State Key Laboratory of Pulp and Paper Engineering, Guangdong Provincial Key Laboratory of Fuel Cell Technology, School of Chemistry and Chemical Engineering, South China University of Technology, Guangzhou 510640, China

[b] CAS Key Laboratory of Science and Technology on Applied Catalysis, Dalian Institute of Chemical Physics, Chinese Academy of Sciences, Dalian 116023, China

[c] University of Chinese Academy of Sciences, Beijing 100049, China

E-mail: fangrq@scut.edu.cn; liyw@scut.edu.cn

Experimental

Chemicals. All chemicals were purchased from commercial sources and directly used without further purification. ($ZrCl_4$, 99.9%, Aladdin), TCPP-Fe (97%, Bidepharm), TCPP-Ni (97%, Bidepharm), 2-phenoxy-1-phenylethanol (98%, Aladdin), 2'-phenoxyacetophenone (99%, Macklin).

Synthesis of PCN-222(Fe/Ni), PCN-222(Fe), and PCN-222(Ni). In a typical synthesis, $ZrCl_4$ (157.2 mg) was dissolved in 20 mL DMF. Then, TCPP-Fe (57.6 mg), TCPP-Ni (6.4 mg), and CF_3COOH (0.9 mL) was added to the above solution, followed by ultrasonication for 10 min. The mixture was transformed into Pyrex vial and heated at 120 °C for 18 h with a heating rate of 10 °C min^{-1}. After naturally cooling to room temperature, the obtained product was centrifuged and washed with DMF for thrice and acetone for twice. The as-obtained precipitates of PCN-222(Fe/Ni) were activated in acetone and finally dried at 70 °C under vacuum overnight.

PCN-222(Fe) was synthesized using the same protocol as PCN-222(Fe/Ni), but the amounts of TCPP-Fe and TCPP-Ni were adjusted to 64 mg and 0 mg, respectively.

PCN-222(Ni) was synthesized using the same protocol as PCN-222(Fe/Ni), but the amounts of TCPP-Fe and TCPP-Ni were adjusted to 0 mg and 64 mg, respectively.

Synthesis of $Fe_3@Ni_1$-ZrO_2, $Fe_3@ZrO_2$, and Ni_1-ZrO_2. Typically, the as-prepared PCN-222(Fe/Ni) was placed in a tubular furnace, which was heated to 600 °C at a ramp rate of 5 °C min^{-1} and kept for 180 min under Ar atmosphere. Before starting to cool down, 3% O_2/Ar was insufflated for 3 min. The obtained powder was denoted as Fe_3@Ni_1-ZrO_2.

Fe_3@ZrO_2 and Ni_1-ZrO_2 were synthesized following the same protocol as Fe_3@Ni_1-ZrO_2, except that the precursors were substituted with PCN-222(Fe) and PCN-222(Ni), respectively.

Synthesis of Ni/Fe-ZrO_2. Typically, the commecial ZrO_2 (268 mg) was immersed in an ethanol solution containing $Ni(OAc)_2\cdot 4H_2O$ (8.3 mg) and $FeCl_3\cdot 6H_2O$ (44 mg), and stirred at room temperature until the ethanol evaporates completely. The as-obtained solid mixture was then ground evenly, and followed by pyrolysis under 600 °C at a ramp rate of 5 °C min^{-1} and kept for 180 min under Ar atmosphere.

Materials characterization. The size and morphology of materials were studied by scanning electron microscopy (SEM) and transmission electron microscopy (TEM). SEM was carried out on a HITACHI SU8220 instrument. TEM and high-angle annular dark-field scanning transmission electron microscopy (HAADF-STEM) were recorded on a FEI Titan Cubed Themis G2 300 S/TEM with a probe corrector and a monochromator at 200 kV. Powder X-ray diffraction (XRD) patterns of the samples were obtained on a Rigaku diffractometer (D/max-IIIA,3 kW) with Cu Kα radiation (λ = 1.5406 Å) at a voltage of 40 kV and a current of 10 mA at room temperature. Brunauer-Emmett-Teller (BET) surface area and pore size measurements were performed on a Micromeritics ASAP 2460 M instrument at 77 K. Before the analysis, the samples were degassed at 150 °C for 12 h. X-ray photoelectron spectroscopy (XPS) was collected on a Thermo Scientific K-Alpha system with the C 1s peak (284.6 eV) as reference. The metal contents of the samples were determined by ICP-OES on an Optima 8300 instrument. Thermogravimetric analysis (TG) was performed on a NETZSCH STA449C instrument loaded with 5 mg sample using a heating rate of 5 °C/min under argon atmosphere. The X-ray absorption experiments were carried out at the Singapore Synchrotron Light Source (SSLS) center. The storage ring was working at the energy of 2.5 GeV with an average electron current of below 200 mA. Si (311) double-crystal was used as the monochromator, and the data was collected using solid-state detector under ambient conditions. The beam size was limited by the horizontal and vertical slits with the area of 1×4 mm^2 during XAS measurements.

Calculation details. Spin-polarized density functional theory (DFT) calculations were performed with the Vienna ab initio simulation package (VASP), using projector augmented wave (PAW) pseudopotential for the core electrons, a cutoff energy of 450 eV for the valence electrons, and the generalized gradient approximation (GGA) in the form of Perdew−Burke−Ernzerhof (PBE) for the exchange correlation potentials. To avoid interactions between adjacent images the c axis of these models is set to be 15 Å. The atoms were relaxed fully until the energy convergence reached 0.00001 eV and the force acting on each atom was less than 0.02 eV/Å. Van der Waals (vdW) interaction was considered at the DFT-D3 level as proposed by Grimme (IVDW = 12). In order to properly localize the Zr 3d states, the DFT + U approach with Ueff = 4 eV was applied to Zr.

Catalytic reactions. In a typical run, 2-phenoxy-1-phenylethanol (**1a**, 1 mmol), 2'-hydroxyacetophenone (**1b**, 1.2 mmol), catalyst (0.05 g), and toluene (3 mL) were sealed in a high-pressure reactor (NSG25-P5-T3-SS1-SV, Anhui Kemi Machinery Technology Co., Ltd). The reactor was evacuated, refilled with air (0.5 MPa), and heated to 150 °C for 30 h under magnetic stirring. After reaction, the reactor was cooled to room temperature. An external standard method was used for quantification with trimethylbenzene as the external standard. The catalyst was isolated by centrifugation and directly reused after washing and drying. The product was identified and quantified by GCMS and GC spectrometer (Agilent, 7890B GC/5977 A MS) equipped with a DB-35 MS UI capillary column (0.25 mm × 30 m).

The conversion and yield were calculated using the following equations:

$$Conversion\ of\ 1a = \left(1 - \frac{Moles\ of\ 1a}{Moles\ of\ 1a\ loaded}\right) \times 100\%$$

$$Yield\ of\ flavone = \left(\frac{Moles\ of\ flavone}{Moles\ of\ 1a\ loaded}\right) \times 100\%$$

The selectivity towards C-C bond cleavage in **1a** was calculated using the following equations:

$$Selectivity\ towards\ C-C\ bond\ cleavage\ =\left(\frac{Moles\ of\ (3a+3b+4a+5a+6a)}{Moles\ of\ 1a\ converted-Moles\ of\ 2a}\right)\times 100\%$$

Note that **2a**, **3a**, **3b**, **4a**, **5a**, and **6a** were shown in Figure 3a.

The selectivity towards aldol condensation between **3a** and **1b** was calculated using the following equation:

$$Selectivity\ towards\ 6a=\left(\frac{Moles\ of\ \ (4a+5a+6a)}{Moles\ of\ (3b+4a+5a+6a)}\right)\times 100\%$$

The turnover number (TON) was calculated using the following equation:

$$TON=\frac{Moles\ of\ 1a\ converted}{Moles\ of\ (Zr+Fe+Ni)}$$

One-pot reaction for flavone production in continuous flow reactor. In a typical run, $Fe_3@Ni_1$-ZrO_2 was pelletized, crushed, and sieved into particles in sizes of 30–50 mesh before filling into the reactor. Specifically, $Fe_3@Ni_1$-ZrO_2 particles (0.5 g) were loaded in the packed column and heated to 180 °C, followed by the feeding of flowing phase (0.2 mmol $_{\text{(2-phenoxy-1-phenylethanol)}}$ / mL $_{\text{(toluene)}}$ and 0.25 mmol $_{\text{(2'-hydroxyacetophenone)}}$ /

mL $_{(toluene)}$) with air bubbling at 50 mL (standard temperature and pressure, STP) min^{-1}. The reaction pressure was held at 1 MPa.

The space time yield (STY) was calculated according to the following equation:

$$STY = \frac{Flavone\ mass}{Catalyst\ mass} \times \frac{1}{Reaction\ time}$$

The turnover frequency (TOF) was calculated using the following equation:

$$TOF = \frac{Moles\ of\ 1a\ converted}{Moles\ of\ (Zr + Fe + Ni)} \times \frac{1}{Reaction\ time}$$

One-pot reaction for acacetin production in continuous flow reactor. In a typical run, $Fe_3@Ni_1$-ZrO_2 was pelletized, crushed, and sieved into particles in sizes of 30–50 mesh before filling into the reactor. Specifically, $Fe_3@Ni_1$-ZrO_2 particles (0.5 g) were loaded in the packed column and heated to 180 °C, followed by the feeding of flowing phase (0.2 mmol $_{(\mathbf{L1}}$ / mL $_{(toluene)}$ and 0.25 mmol $_{(Phloracetophenone,\ \mathbf{P3})}$ / mL $_{(toluene)}$) with air bubbling at 50 mL (standard temperature and pressure, STP) min^{-1}. The reaction pressure was held at 1 MPa.

The space time yield (STY) was calculated according to the following equation:

$$STY = \frac{Acacetin\ mass}{Catalyst\ mass} \times \frac{1}{Reaction\ time}$$

The turnover frequency (TOF) was calculated using the following equation:

$$TOF = \frac{Moles\ of\ L1\ converted}{Moles\ of\ (Zr + Fe + Ni)} \times \frac{1}{Reaction\ time}$$

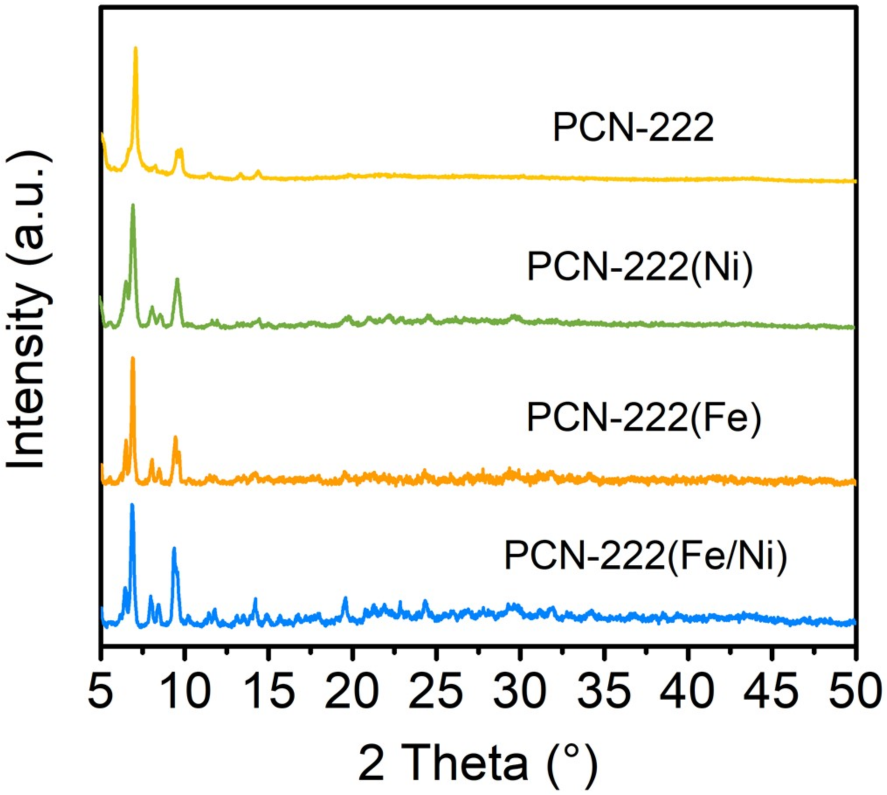

Figure S1. XRD patterns of the as-synthesized PCN-222(Fe/Ni), PCN-222(Fe), PCN-222(Ni), and PCN-222.

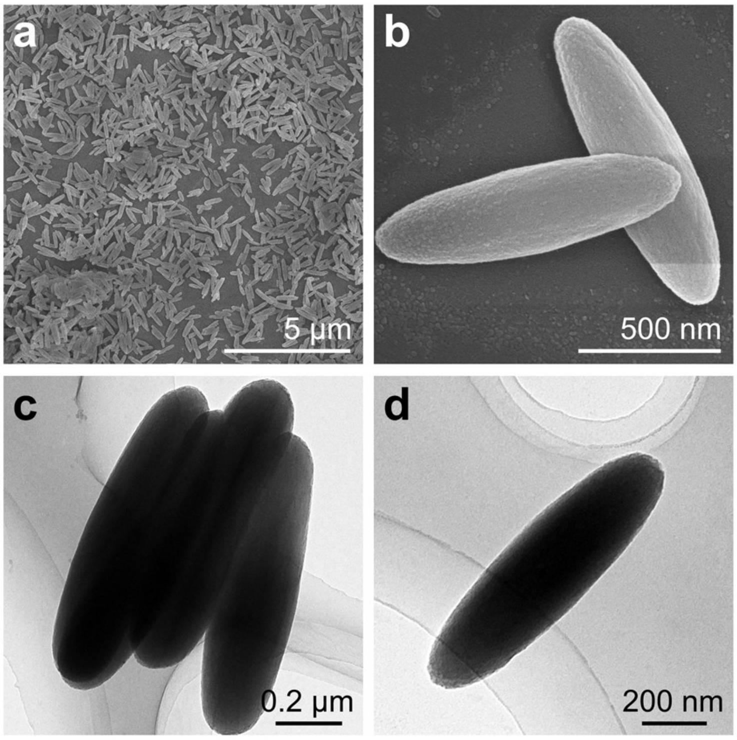

Figure S2. (a, b) SEM and (c, d) TEM images of the as-synthesized PCN-222(Fe/Ni).

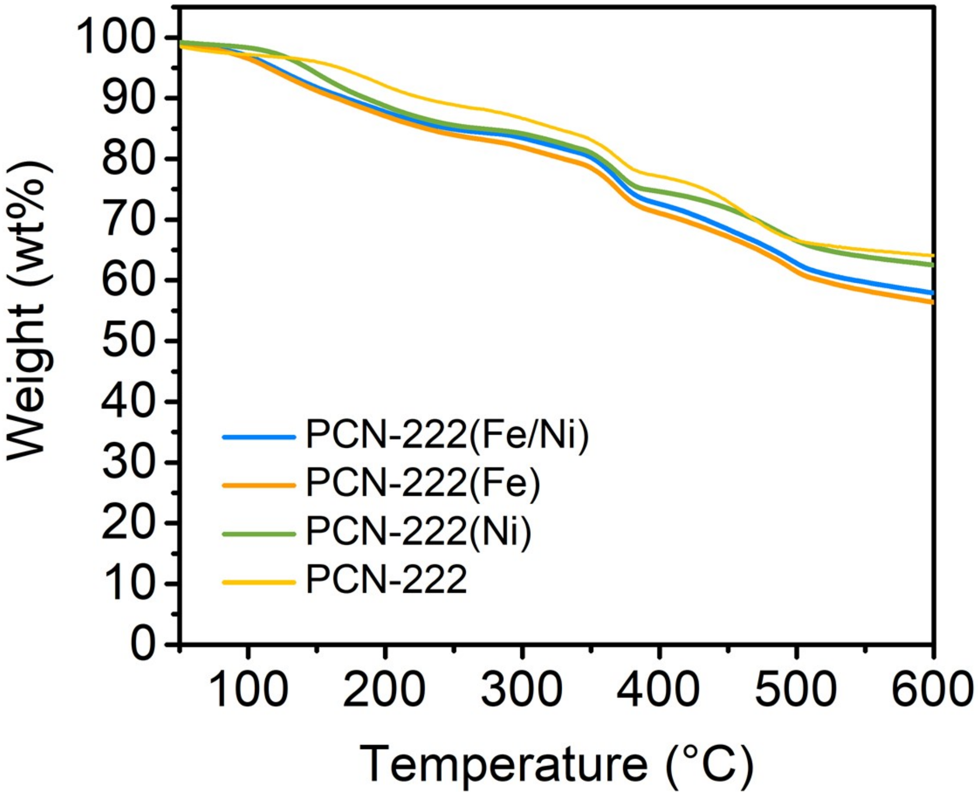

Figure S3. TGA curves of the as-synthesized PCN-222(Fe/Ni), PCN-222(Fe), PCN-222(Ni), and PCN-222 under N_2 atmosphere.

The slight difference between the thermogravimetric curves of the four PCN-222 samples is due to the subtle differences in the organic ligands used in their preparation process.

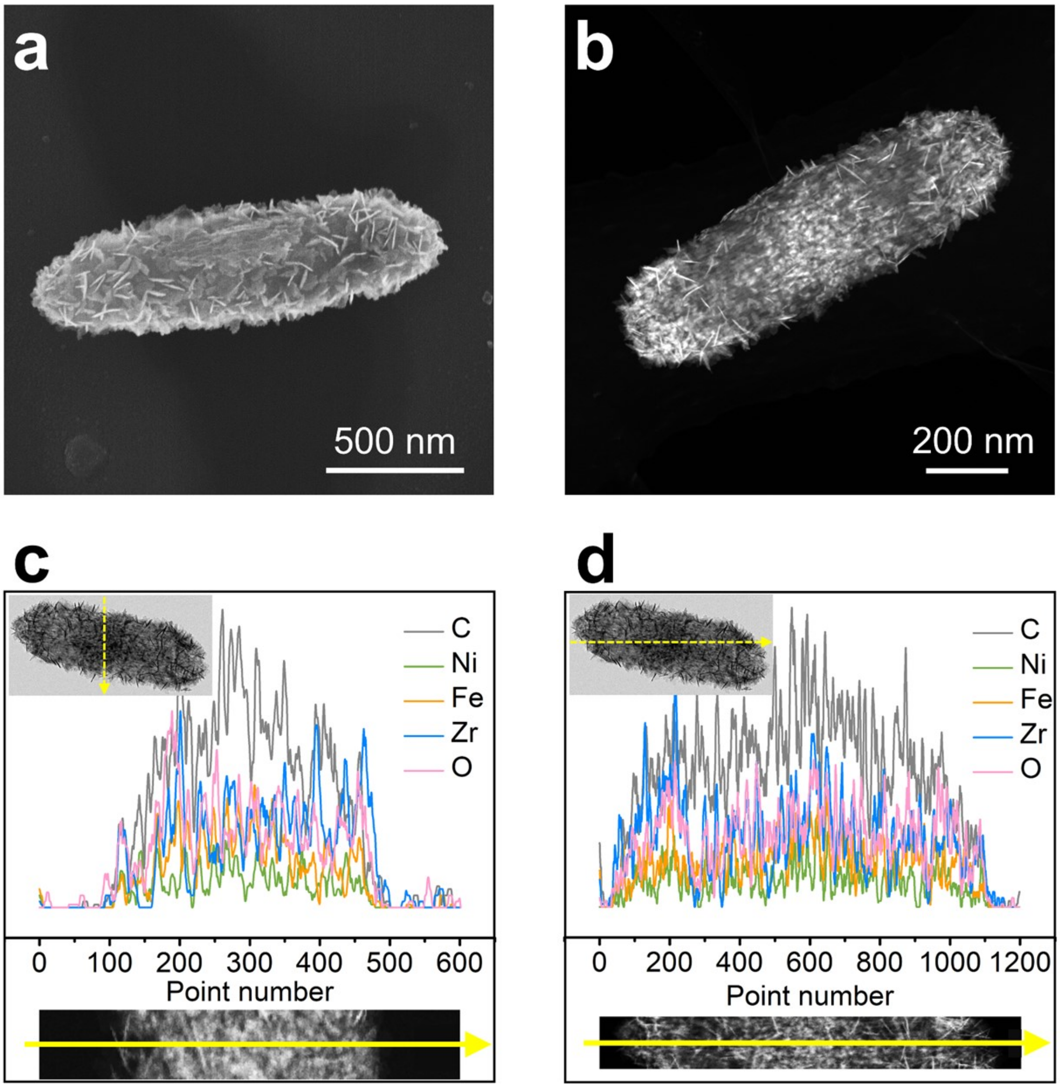

Figure S4. (a) SEM image, (b) HAADF-STEM image, (c, d) elemental line scanning profiles of $Fe_3@Ni_1\text{-}ZrO_2$.

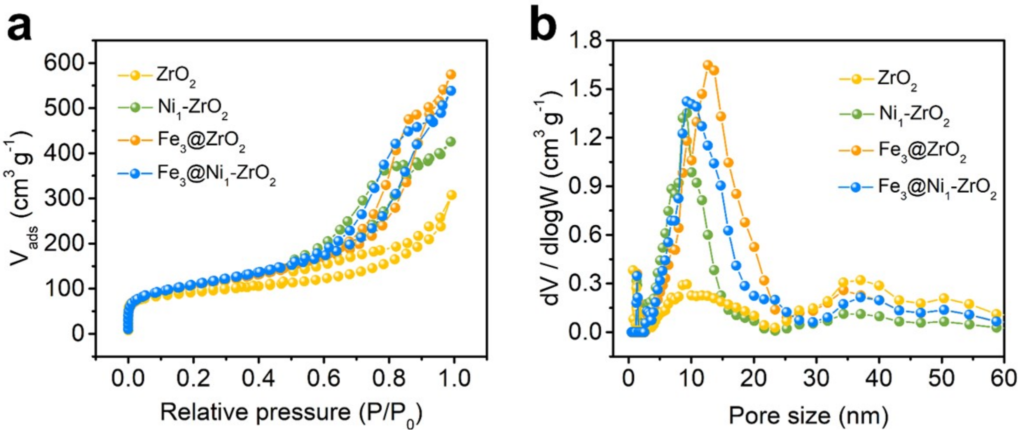

Figure S5. (a) N_2 adsorption-desorption isotherms, and (b) corresponding pore-size distributions of Fe_3@Ni_1-ZrO_2, Fe_3@ZrO_2, Ni_1-ZrO_2, and ZrO_2.

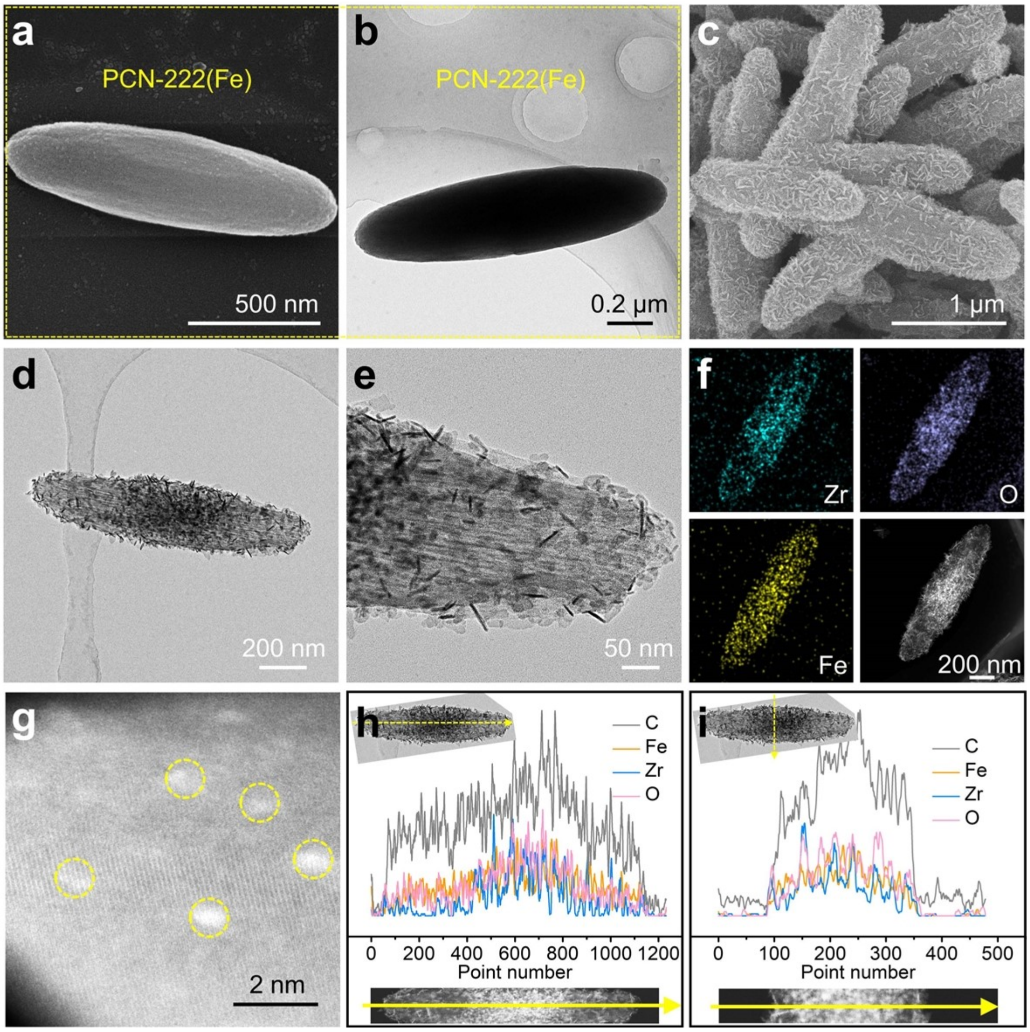

Figure S6. (a) SEM and (b) TEM images of PCN-222(Fe). (c) SEM, (d, e) TEM, (f) corresponding elemental mapping, (g) AC HAADF-STEM images, and (h, i) elemental line scanning profiles of the as-synthesized $Fe_3@ZrO_2$.

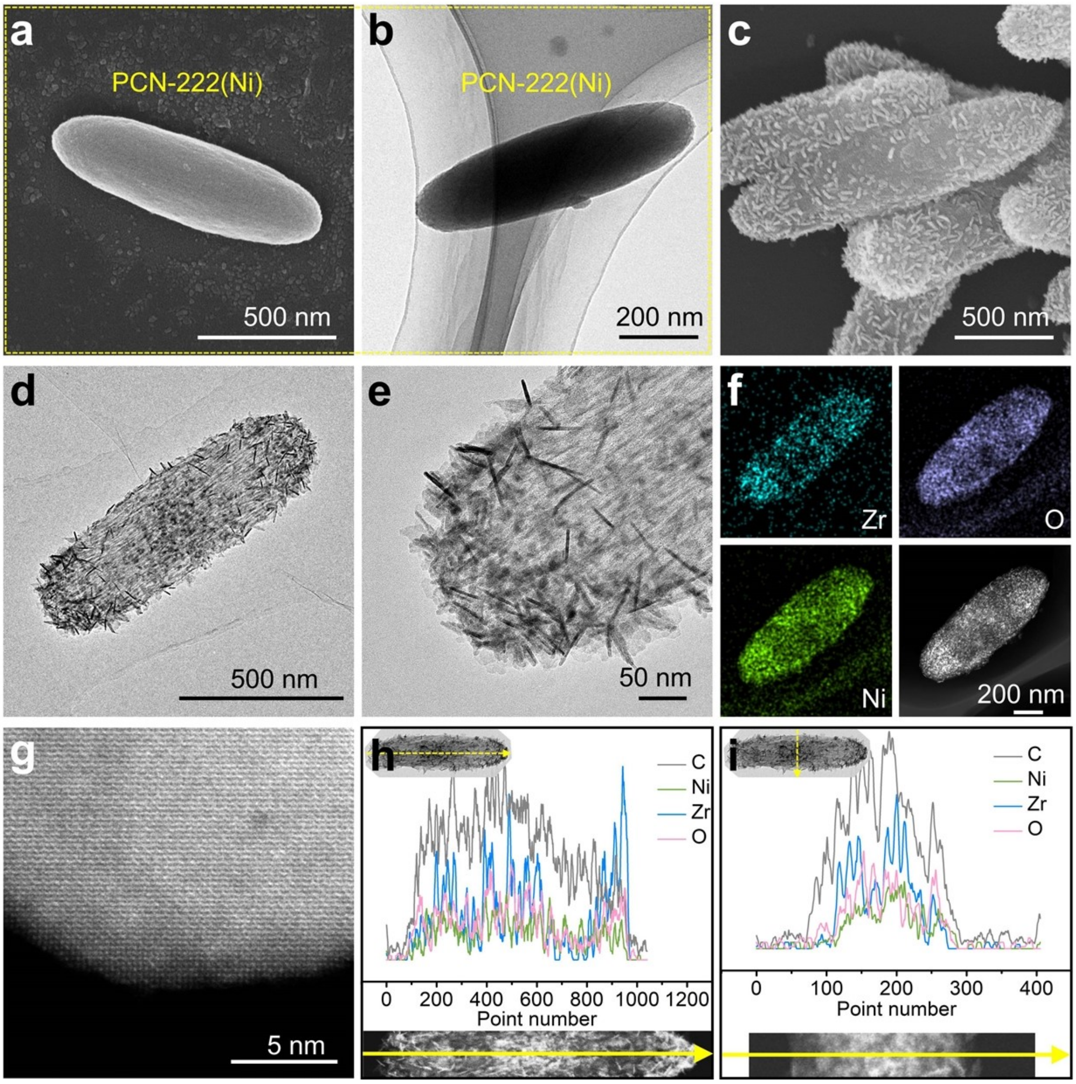

Figure S7. (a) SEM and (b) TEM images of PCN-222(Ni). (c) SEM, (d, e) TEM, (f) corresponding elemental mapping, (g) AC HAADF-STEM images, and (h, i) elemental line scanning profiles of the as-synthesized Ni_1-ZrO_2.

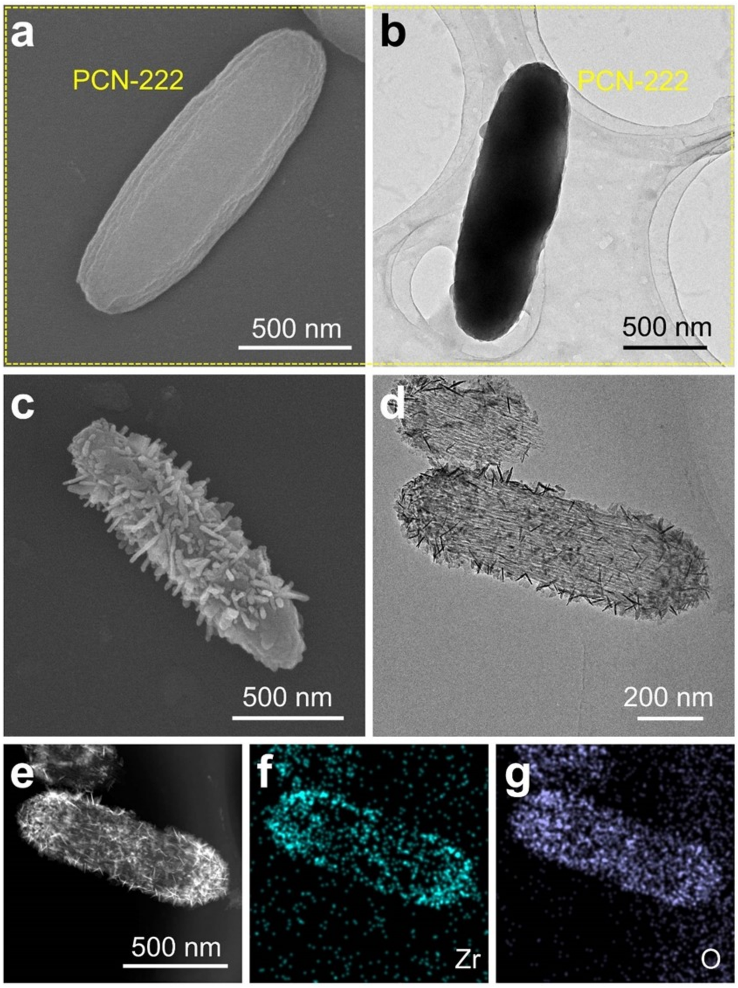

Figure S8. (a) SEM and (b) TEM images of PCN-222. (c) SEM, (d) TEM, (e) AC HAADF-STEM, and (f, g) corresponding elemental mapping images of the as-synthesized ZrO_2.

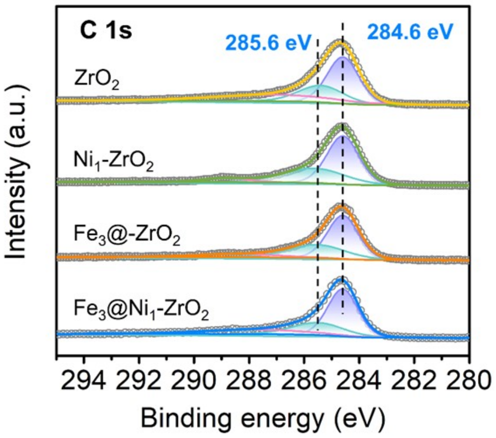

Figure S9. XPS spectra in C 1s region of Fe_3@Ni_1-ZrO_2, Fe_3@ZrO_2, Ni_1-ZrO_2, and ZrO_2.

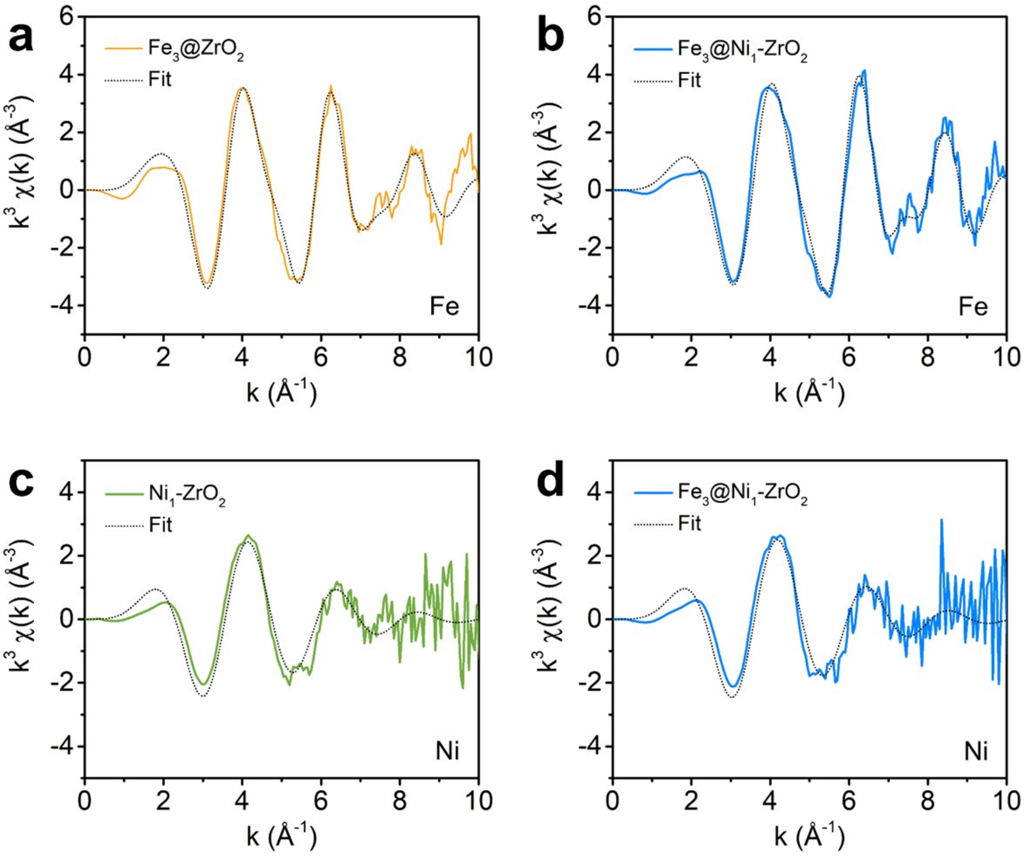

Figure S10. Fe *K*-edge EXAFS fitting curves of (a) Fe_3@ZrO_2 and (b) Fe_3@Ni_1-ZrO_2. Ni *K*-edge EXAFS fitting curves of (c) Ni_1-ZrO_2, and (d) Fe_3@Ni_1-ZrO_2.

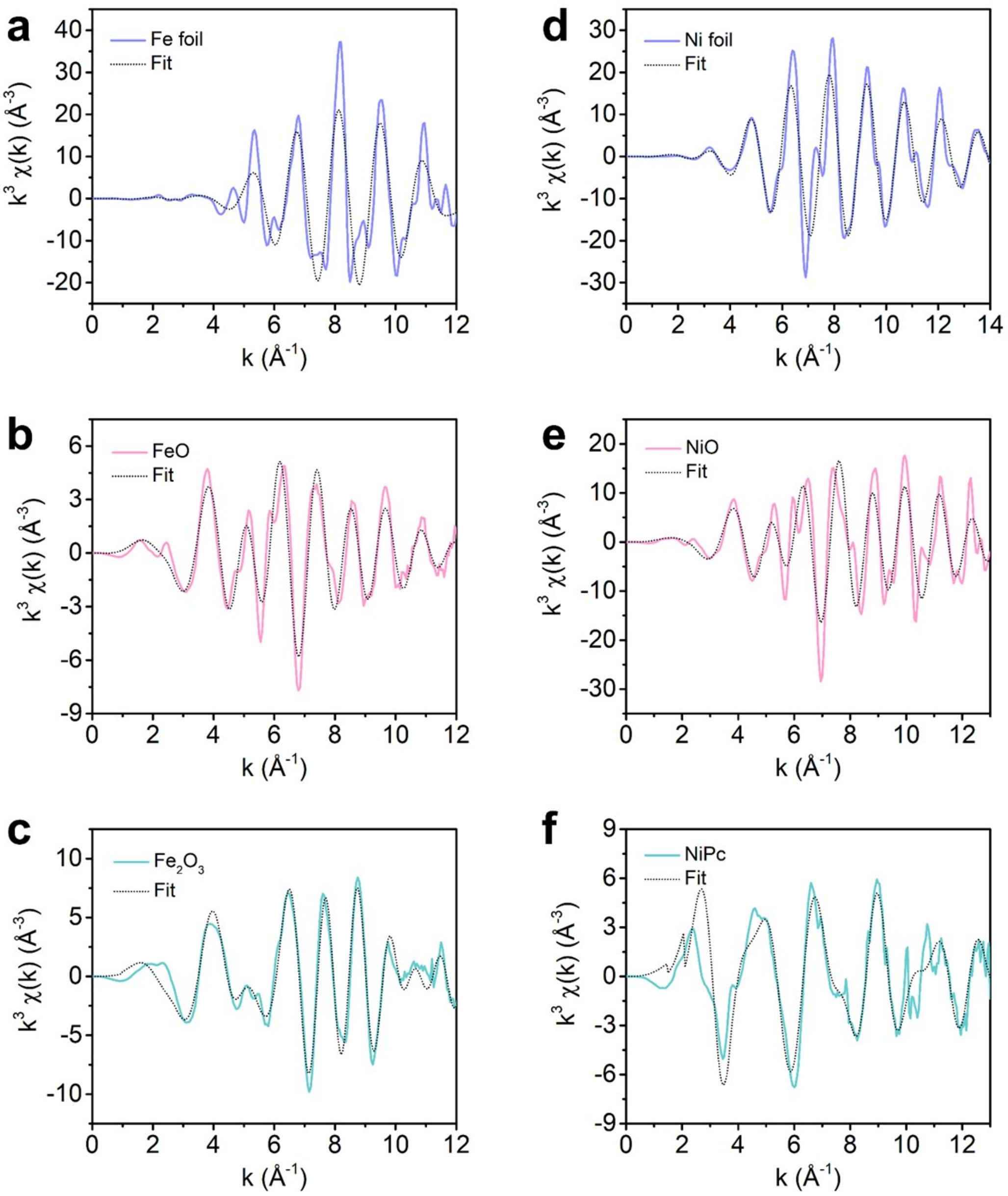

Figure S11. Fe *K*-edge EXAFS fitting curves of (a) Fe foil, (b) FeO, and (c) Fe_2O_3. Ni *K*-edge EXAFS fitting curves of (a) Ni foil, (b) NiO, and (c) NiPC.

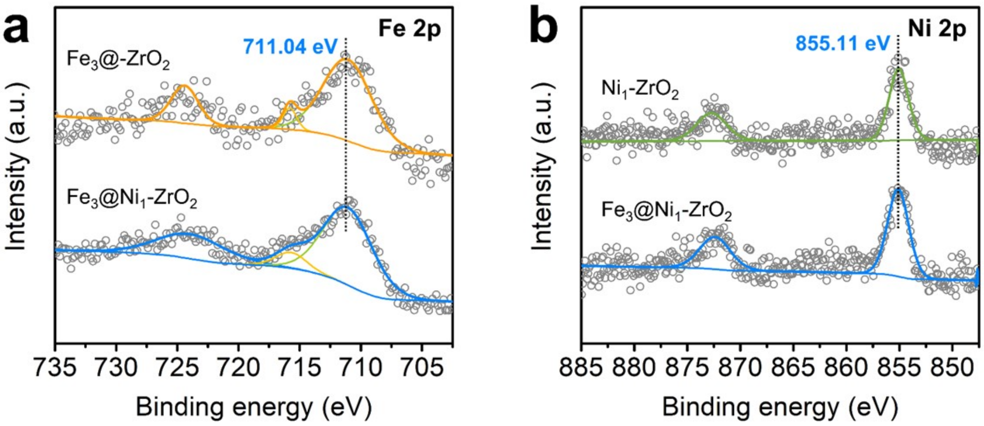

Figure S12. (a) Fe 2p spectra, and (b) Ni 2p spectra of Fe_3@Ni_1-ZrO_2, Fe_3@ZrO_2, and Ni_1-ZrO_2.

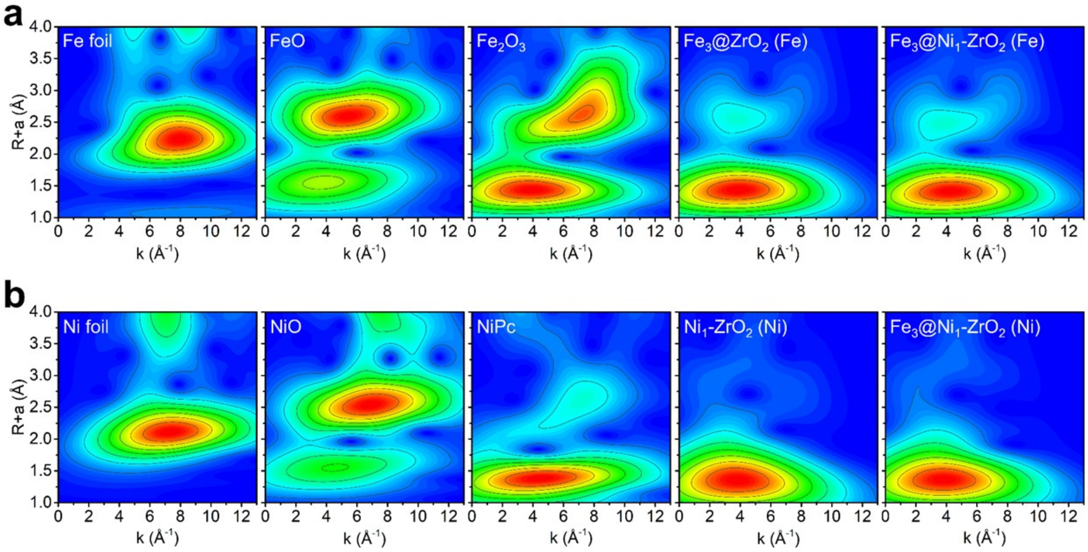

Figure S13. WT k^3-weighted EXAFS spectra.

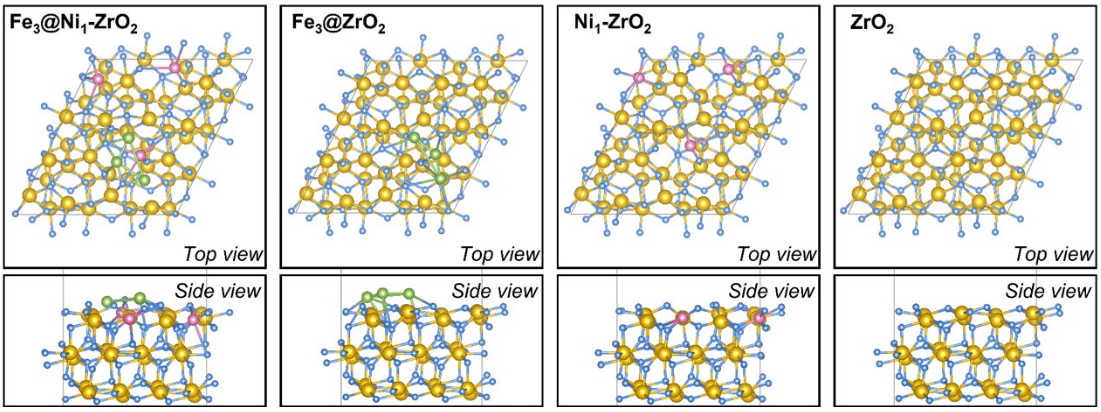

Figure S14. The optimized DFT models of Fe_3@Ni_1-ZrO_2, Fe_3@ZrO_2, Ni_1-ZrO_2, and ZrO_2. The yellow, blue, green, and pink balls represent Zr, O, Fe, and Ni atoms, respectively.

The initial ZrO_2 surface model consists of 136 atoms, of which 88 are oxygen atoms. Considering that the presence of oxygen vacancies in the as-synthesized samples, four oxygen atoms were removed to achieve a concentration of 4.5% of oxygen vacancies in the models.

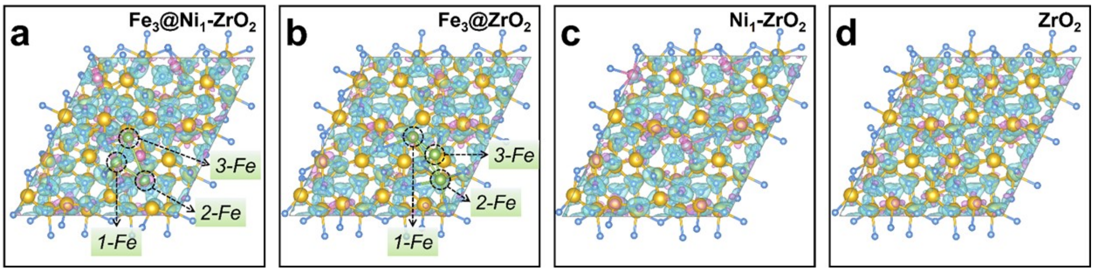

Figure S15. Top view of the differential charge densities of (a) $Fe_3@Ni_1-ZrO_2$, (b) $Fe_3@ZrO_2$, (c) Ni_1-ZrO_2, and (d) ZrO_2; cyan and pink isosurfaces with an isosurface level of 0.015 e/a_0^3 represent electron accumulation and depletion areas, respectively.

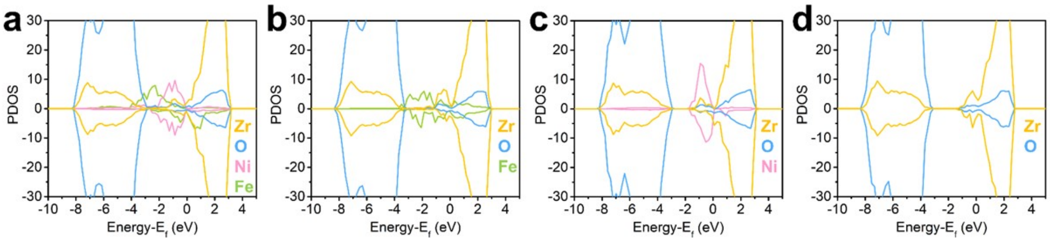

Figure S16. Project density of states (*p*DOS) of (a) $Fe_3@Ni_1\text{-}ZrO_2$, (b) $Fe_3@ZrO_2$, (c) $Ni_1\text{-}ZrO_2$, and (d) ZrO_2.

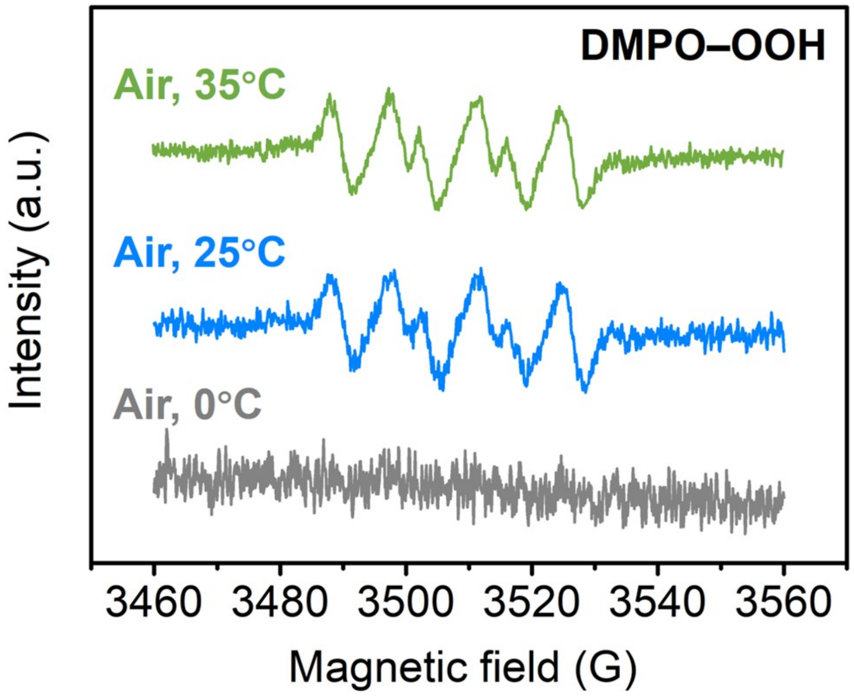

Figure S17. *In-situ* EPR spectra during the one-pot multistep oxidation process.

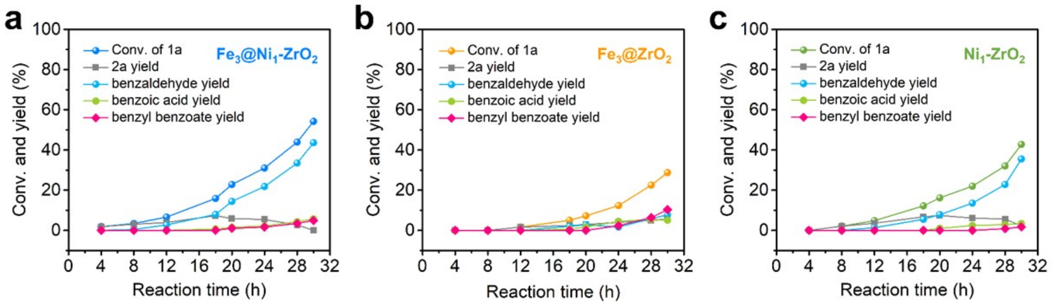

Figure S18. Control experiments using 2-phenoxy-1-phenylethanol (**1a**) as the only substrate. Reaction conditions: 2-phenoxy-1-phenylethanol (**1a**, 1 mmol), catalyst (0.05 g), toluene (3 mL), 150 °C, 30 h, air (0.5 MPa).

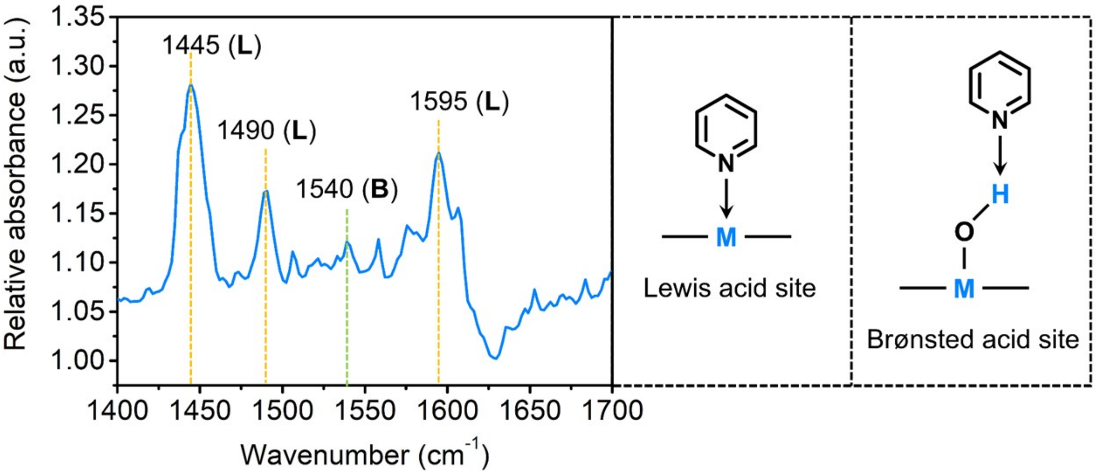

Figure S19. Py-FTIR spectra of Fe_3@Ni_1-ZrO_2 and the schematic illustration of the Lewis and Brønsted acid sites.

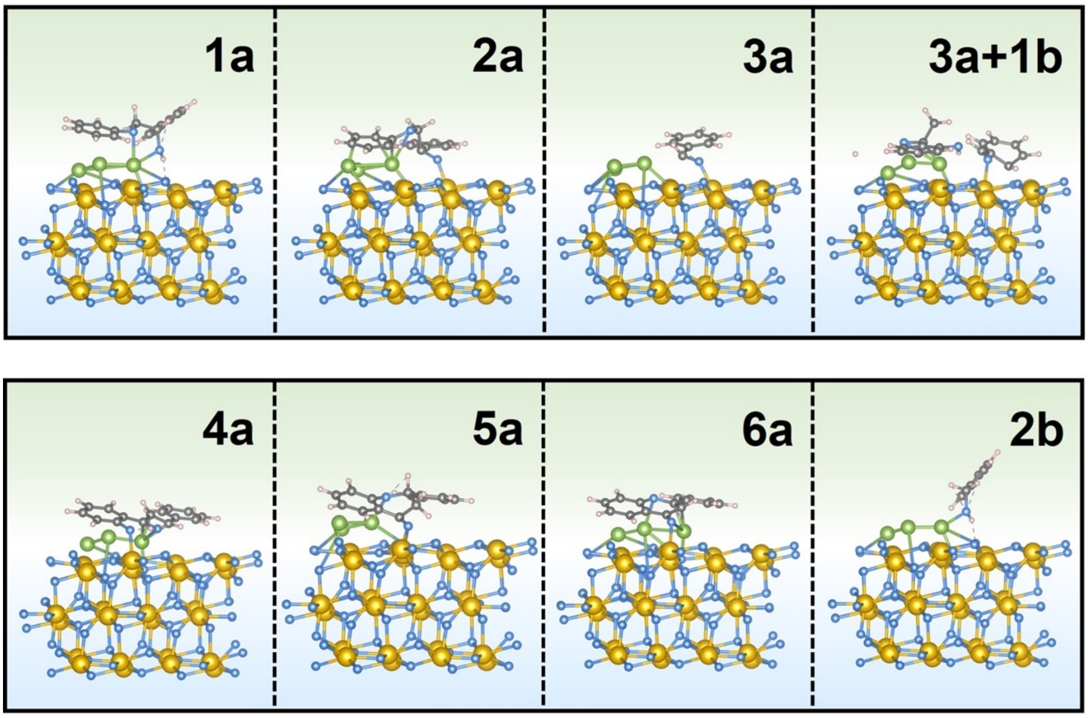

Figure S20. The simplified surface structures of various reaction species along the reaction pathway over $Fe_3@ZrO_2$. Fe (blue), Zr (cyan), O (red), C (gray), and H (white).

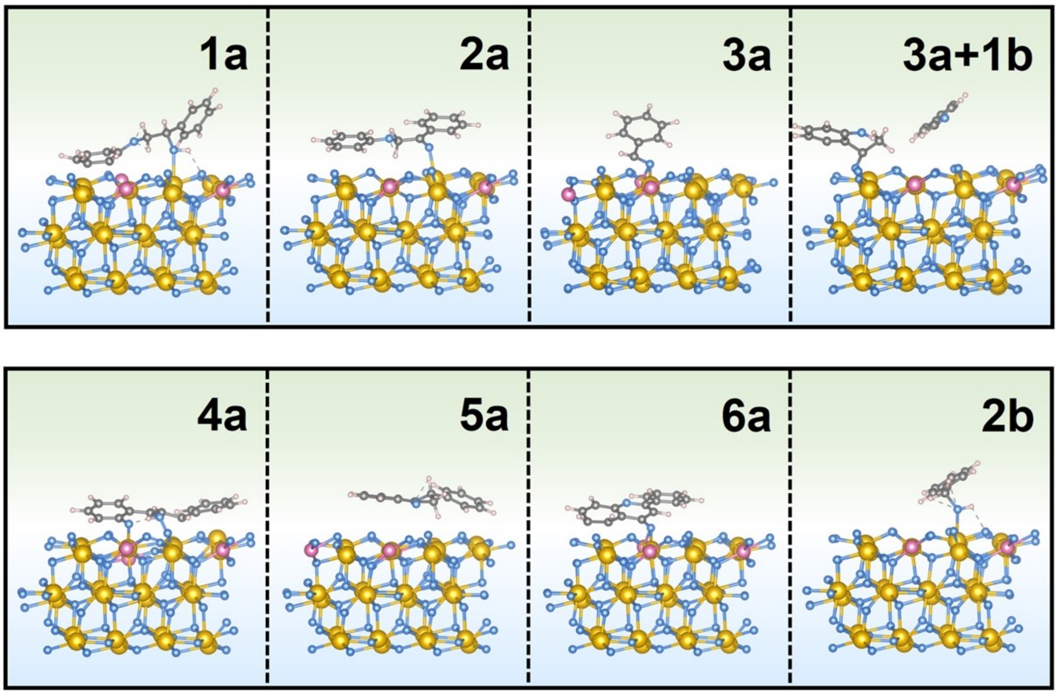

Figure S21. The simplified surface structures of various reaction species along the reaction pathway over Ni_1-ZrO_2. Ni (purple), Zr (cyan), O (red), C (gray), and H (white).

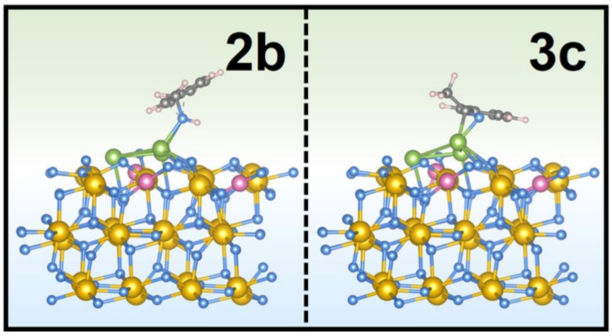

Figure S22. The simplified surface structures of various reaction species along the reaction pathway over Fe_3@Ni_1-ZrO_2. Fe (blue), Ni (purple), Zr (cyan), O (red), C (gray), and H (white).

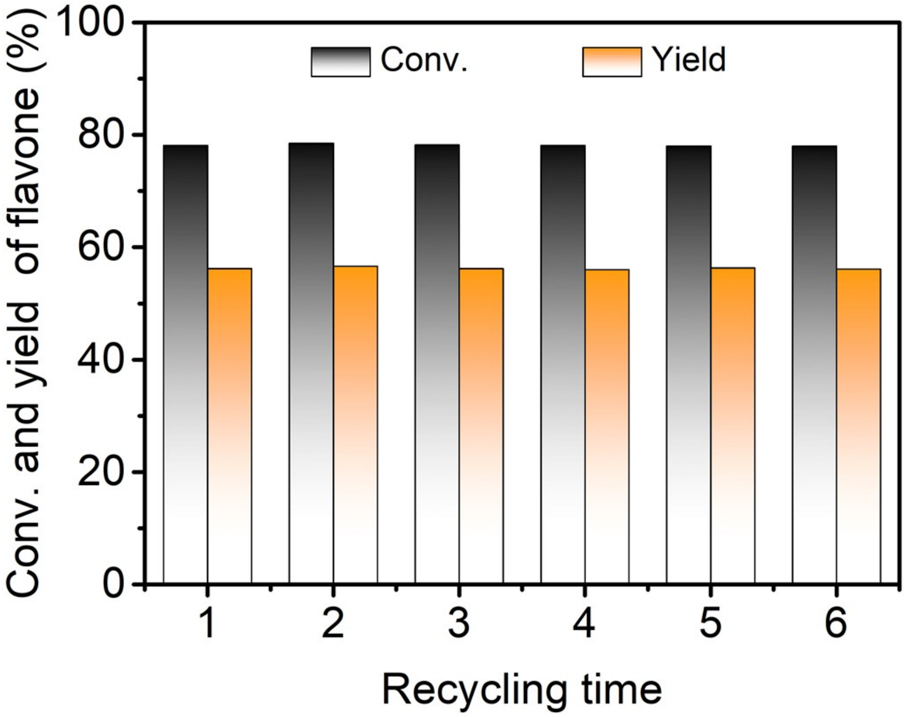

Figure S23. Reusability examination of the $Fe_3@Ni_1$-ZrO_2 in the one-pot oxidative tandem reaction. Reaction conditions: 2-phenoxy-1-phenylethanol (**1a**, 1 mmol), 2'-hydroxyacetophenone (**1b**, 1.2 mmol), catalyst (0.05 g), toluene (3 mL), 150 °C, 30 h, air (0.5 MPa).

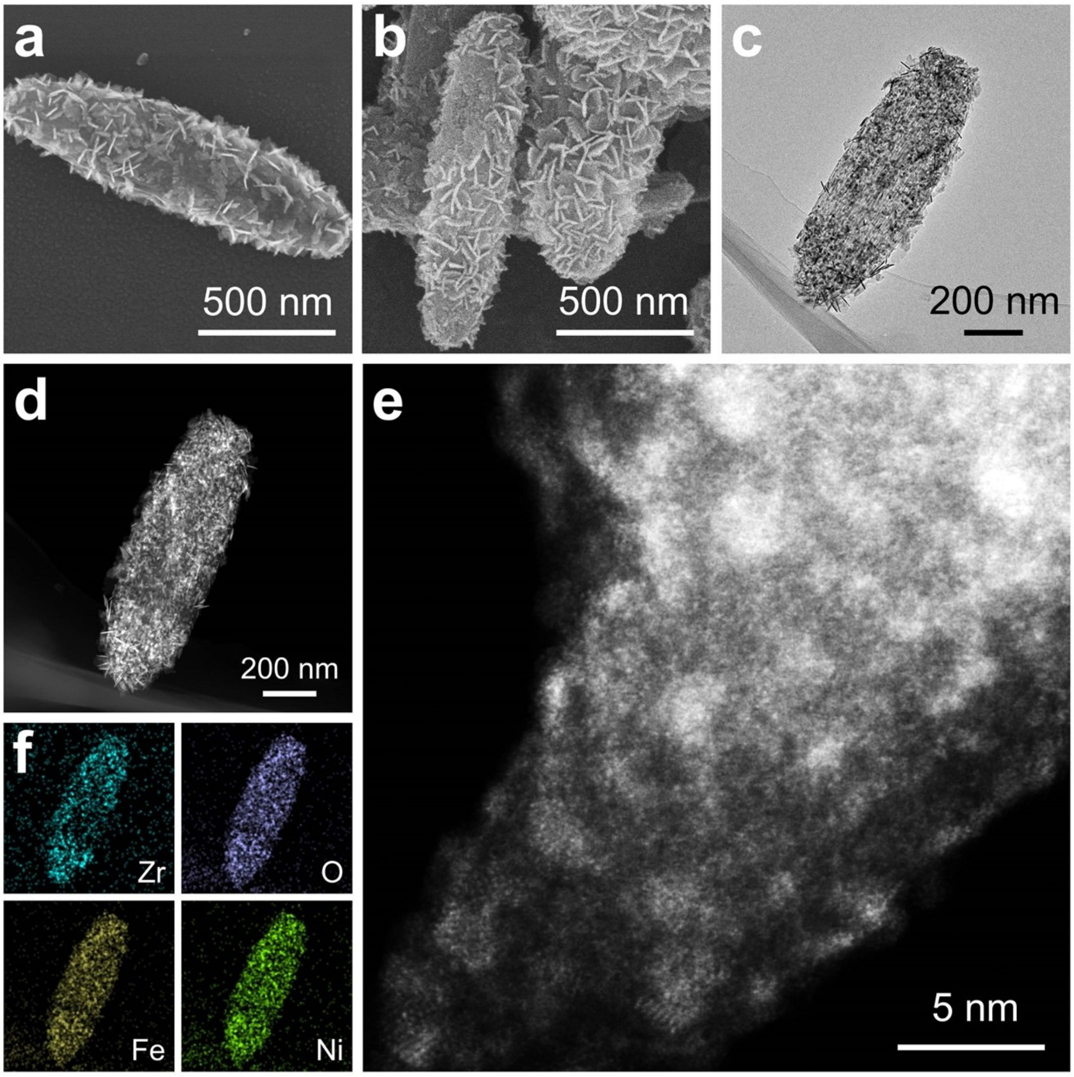

Figure S24. (a, b) SEM, (c) TEM, (d) HAADF-STEM, (e) AC HAADF-STEM, and (f) corresponding elemental mapping images of the recycled $Fe_3@Ni_1-ZrO_2$.

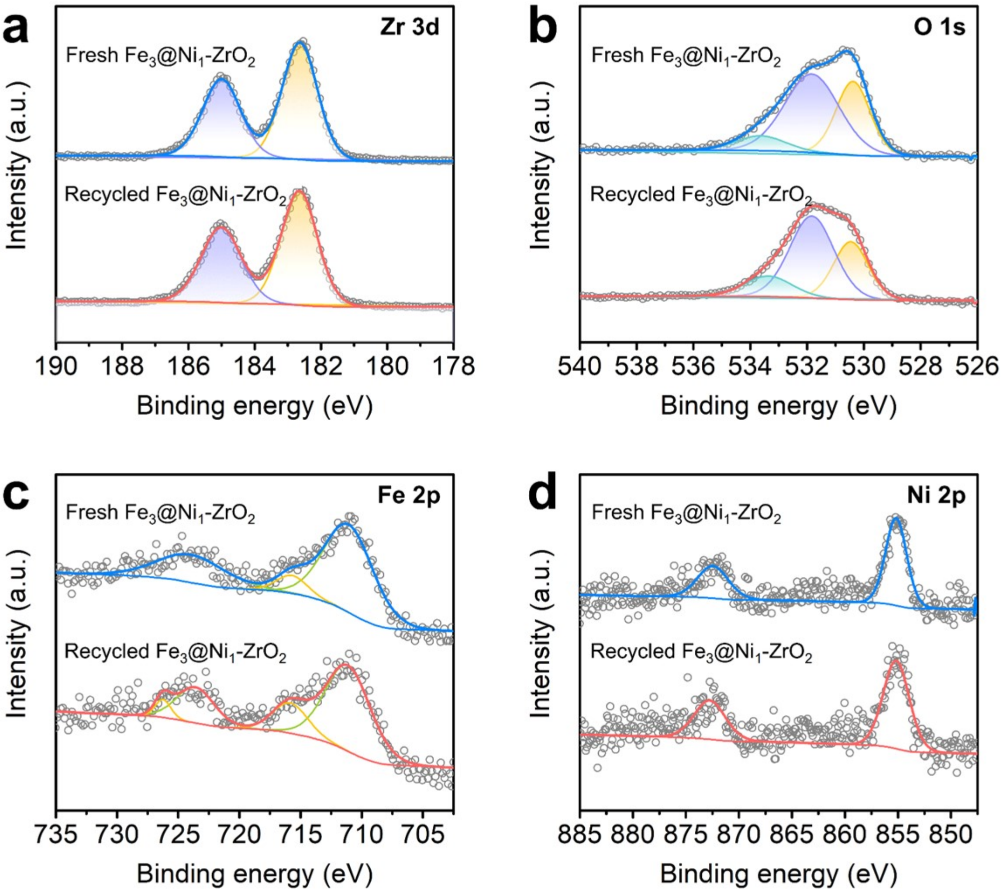

Figure S25. XPS analysis of Zr 3d, O 1s, Fe 2p, and Ni 2p region of the recycled $Fe_3@Ni_1$-ZrO_2.

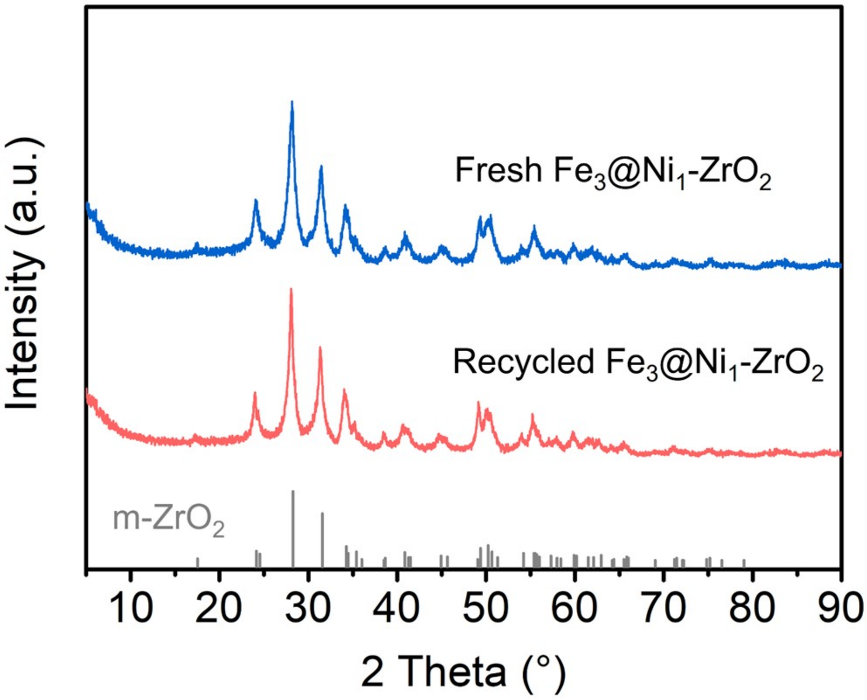

Figure S26. XRD patterns of the recycled Fe$_3$@Ni$_1$-ZrO$_2$.

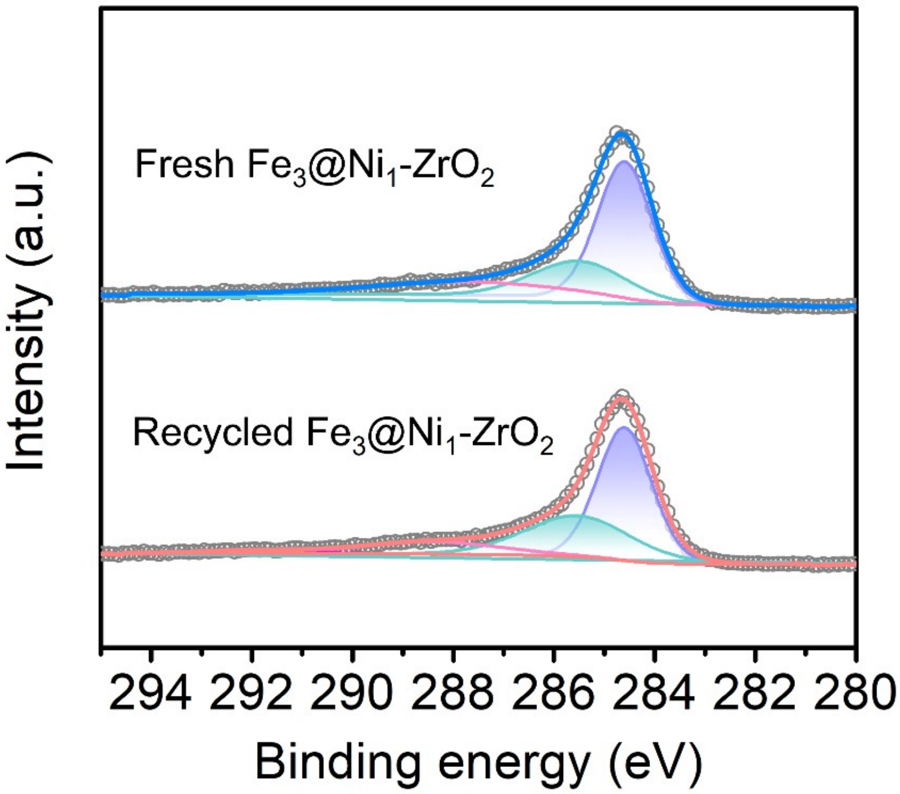

Figure S27. XPS analysis of C 1s region of the recycled $Fe_3@Ni_1$-ZrO_2.

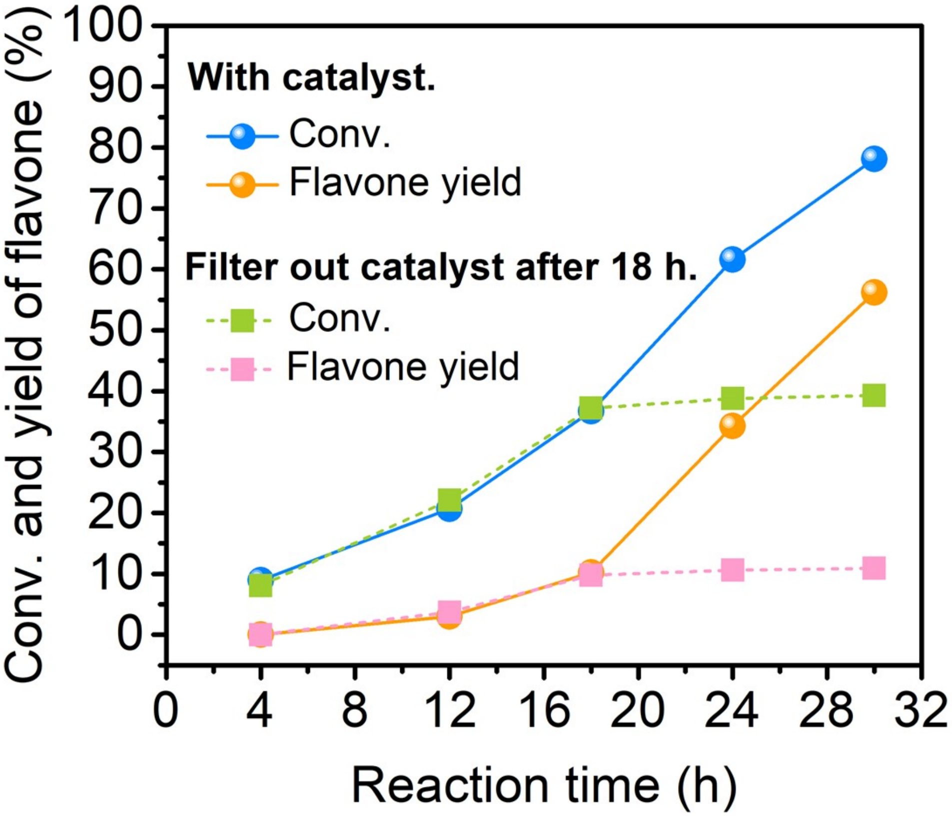

Figure S28. The hot filtration experiment results for the one-pot oxidative tandem reaction over $Fe_3@Ni_1$-ZrO_2. Reaction conditions: 2-phenoxy-1-phenylethanol (**1a**, 1 mmol), 2'-hydroxyacetophenone (**1b**, 1.2 mmol), catalyst (0.05 g), toluene (3 mL), 150 °C, 30 h, air (0.5 MPa).

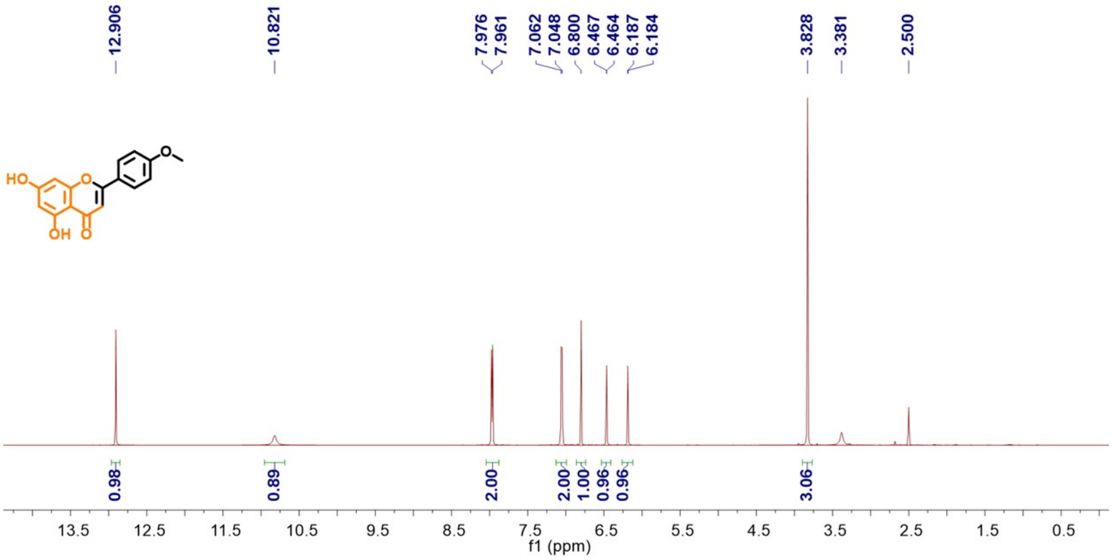

Figure S29. ^{1}H NMR (600 MHz, DMSO-d6) δ 12.906 (brs, 1H), 10.821 (brs, 1H), 7.968 (d, J = 9.0 Hz, 2H), 7.055 (d, J = 8.4 Hz, 2H), 6.800 (s, 1H), 6.466 (d, J = 1.8 Hz, 1H), 6.186 (d, J = 1.8 Hz, 1H), 3.828 (s, 3H).

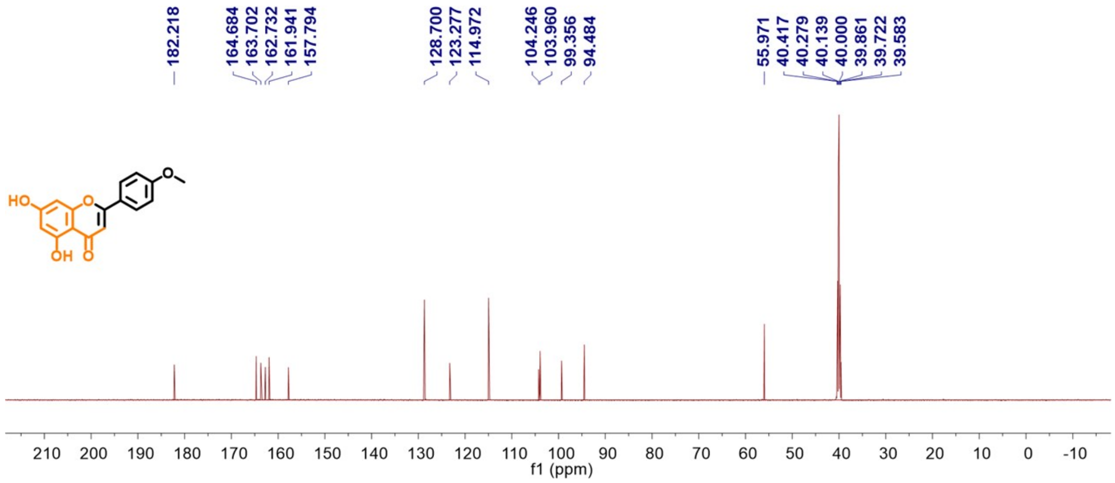

Figure S30. ^{13}C NMR (151 MHz, DMSO-d6) δ 182.22, 164.68, 163.70, 162.73, 161.94, 157.79, 128.70, 123.28, 114.97, 104.25, 103.96, 99.36, 94.48, 55.97.

Table S1. Characterization results of the as-synthesized samples.

Sample	S_{BET} ($m^2\ g^{-1}$)	Pore volume ($cm^3\ g^{-1}$)	Element contents (wt%)			
			Zr	Fe	Ni	C
$Fe_3@Ni_1$-ZrO_2	377.8	0.81	26.8	4.4	0.83	52.5
$Fe_3@ZrO_2$	362.0	0.79	26.3	4.3	–	53.4
Ni_1-ZrO_2	366.4	0.64	28.9	–	1.36	56.4
ZrO_2	335.4	0.40	29.3	–	–	54.3
Recycled $Fe_3@Ni_1$-ZrO_2	383.6	0.80	26.4	4.5	0.81	53.3

Table S2. EXAFS fitting parameters at the Fe K-edge (S_0^2=0.67).

Sample	Path	C.N.	R (Å)	$\sigma^2 \times 10^{-3}$ (Å^2)	ΔE (eV)	R factor
Fe foil	Fe–Fe	8*	2.45±0.01	1.0±2.6	2.3±3.1	0.010
	Fe–Fe	6*	2.84±0.01	1.8±3.4	2.0±6.0	
FeO	Fe–O	5.7±1.4	2.12±0.02	11.7±3.1	0.6±2.8	0.008
	Fe–Fe	12.2±1.7	3.08±0.01	11.4±1.2	1.3±1.4	
Fe_2O_3	Fe–O	6.4±1.4	1.96±0.02	12.9±2.7	−7.4±3.1	0.009
	Fe–Fe	6.3±1.1	3.00±0.01	8.8±1.4	3.6±1.8	
	Fe–Fe	2.6±0.9	3.67±0.02	2.3±2.0	−7.9±3.2	
Fe_3@Ni_1-ZrO_2	Fe–O	6.2±0.8	1.98±0.01	10.4±.6	−3.0±1.4	0.012
	Fe–Fe	3.5±2.0	3.08±0.04	15.1±6.0	0.5±4.3	
Fe_3@ZrO_2	Fe–O	6.4±0.6	2.00±0.01	12.7±1.5	−0.6±1.0	0.005
	Fe–Fe	6.8±3.3	3.09±0.01	25.2±6.4	1.0±0.4	

C.N.: coordination numbers; R: bond distance; σ^2: Debye-Waller factors; ΔE: the inner potential correction. R factor: goodness of fit. *Fitting with fixed parameter.

Table S3. EXAFS fitting parameters at the Ni K-edge (S_0^2=0.77).

Sample	Path	C.N.	R (Å)	$\sigma^2 \times 10^{-3}$ (Å^2)	ΔE (eV)	R factor
Ni foil	Ni–Ni	12*	2.48±0.01	5.9±0.3	−4.2±0.6	0.002
NiO	Ni–O	6.0±0.7	2.08±0.01	5.2±0.9	−1.4±1.6	0.004
	Ni–Ni	12.6±0.7	2.95±0.01	6.0±0.3	−3.0±0.6	
Fe_3@Ni_1-ZrO_2	Ni–O	6.1±2.1	1.92±0.03	22.0±5.9	−7.6±3.3	0.012
Ni_1-ZrO_2	Ni–O	6.5±1.8	1.94±0.02	23.6±4.8	−7.6±2.5	0.007

C.N.: coordination numbers; R: bond distance; σ^2: Debye-Waller factors; ΔE: the inner potential correction. R factor: goodness of fit. *Fitting with fixed parameter.

Table S4. Catalytic performance for the as-synthesized catalysts. [a]

Entry	Catalyst	Conv. (%)	TON	[c] Sele. (%)	[d] Sele. (%)	Yield (%)						
						2a	3a	4a	5a	**6a**	3b	Anisole
1	None	2.1	–	–	–	2.1	–	–	–	–	–	–
2	Fe_3@Ni_1-ZrO_2	78.1	4.04	100	93.8	4.0	3.2	5.3	5.0	**56.2**	4.4	72.0
3[b]	Fe_3@Ni_1-ZrO_2	–	–	–	–	–	–	–	–	–	–	–
4	Fe_3@ZrO_2	53.6	2.93	85.0	62.6	4.1	4.9	7.1	9.9	**6.3**	13.9	46.6
5	Ni_1-ZrO_2	62.1	3.70	100	0	28.3	32.6	–	–	–	1.2	30.5
6	ZrO_2	33.6	2.10	37.3	–	17.8	5.9	–	–	–	–	13.3
7	C-ZrO_2	21.7	0.40	35.8	–	9.4	4.4	–	–	–	–	9.9
8	Fe/Ni-C-ZrO_2	69.8	1.16	75.7	32.7	14.7	16.3	8.3	–	–	17.1	51.4

[a] Reaction conditions: 2-phenoxy-1-phenylethanol (**1a**, 1 mmol), 2’-hydroxyacetophenone (**1b**, 1.2 mmol), catalyst (0.05 g), toluene (3 mL), 150 °C, 30 h, air (0.5 MPa). [b] N_2 (0.5 MPa). [c] Selectivity of C-C cleavage. [d] Selectivity of aldol condensation.

Table S5. Yields of different components generated during the proposed one-pot cascade catalytic system over $Fe_3@Ni_1-ZrO_2$. [a]

Reaction time (h)	Conv. (%)	Yield (%)					
		2a	**3a**	**4a**	**5a**	**6a**	**3b**
4	9.0	6.1	2.9	–	–	–	–
12	20.8	11.5	3.9	1.3	–	3.0	1.1
18	36.7	14.8	5.0	2.9	2.0	10.2	1.8
24	61.7	8.8	9.6	3.6	2.5	34.3	2.9
30	78.1	4.0	3.2	5.3	5.0	56.2	4.4

[a] Reaction conditions: 2-phenoxy-1-phenylethanol (**1a**, 1 mmol), 2'-hydroxyacetophenone (**1b**, 1.2 mmol), catalyst (0.05 g), toluene (3 mL), 150 °C, air (0.5 MPa).

Table S6. Reported catalytic systems for bond cleavage of lignin β-O-4 model compounds.

Substrate, reaction conditions, and catalysts	Conv. (%)	Sele. (%)	Additives	Ref.
Guaiacyl glycerol-β-guaiacyl ether H_2 (3 MPa), 180 °C,4 h. Mo_1Al/MgO (Al Lewis acid sites)	91	–	–	S1
2-Phenoxy-1-phenylethanol TBHP (0.5 mmol), MeCN (1.0 mL), RT, 5 h, under air, electrolysis under current of 20 mA and potential of 5.0 V vs Ag/AgCl. Pt NPs/N-CNTs	62	40 toward C-C cleavage	*n*Bu_4NOH	S2
2-Phenoxy-1-phenylethanol TBHP (0.5 mmol), MeCN (1.0 mL), RT, 5 h, under air, electrolysis under current of 20 mA and potential of 5.0 V vs Ag/AgCl. Pt_1+NP/CNTs	77	47 toward C-C cleavage	*n*Bu_4NOH	S2
2-(2-methoxyphenoxy)-1-phenylethanol Base (0.8 mmol), solvent (2 mL), 140 °C, t=20 h under air.	100	–	NaOH	S3
2-(2-methoxyphenoxy)-1-phenylethanol Base (0.8 mmol), solvent (2 mL), 140 °C, t=20 h under air.	89	–	KOH	S3
2-(2-methoxyphenoxy)-1-phenylethanol Base (0.8 mmol), solvent (2 mL), 140 °C, t=20 h under air.	100	–	*t*-BuOK	S3
2-(2-Methoxyphenoxy)-1-phenylethanol Base (0.8 mmol), solvent (2 mL), 140 °C,	14	–	Cs_2CO_3	S3

t=20 h under air. 2-Phenoxy-1-phenylethanol Solvent 2 mL, 0.05 mmol (1.0 equiv.) 0.5 W cm^{-2} intensity of LED light for photoreactions with results shown in red and results of dark reactions shown in blue.	96	–	hydrazine hydrate	S4
Ni/ZrO$_2$ 2-(2-Methoxyphenoxy)-1-phenylethanol Tert-amyl alcohol (4.0 mL) were mixed in the air at 110 °C, reaction time (t) = 20 h.	–	–	NaOH	S5

Table S7. Reported catalytic systems for flavonoid synthesis.

Reaction and conditions	Yield (%)	Additive	Ref.
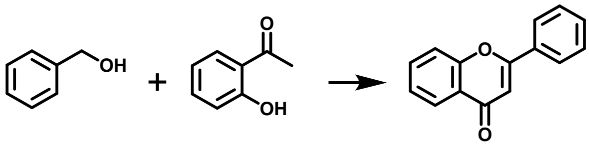 120 °C, 12 h, O_2 (2 bar), *n*-hexanol (4 mL).	99	K_2CO_3	S6
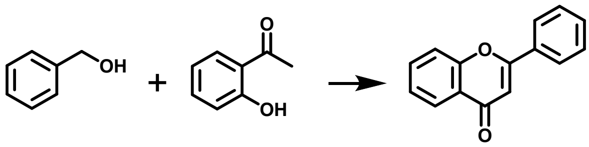 130 °C, 20 h, O_2 (2 bar), *n*-hexanol (4 mL).	99	K_2CO_3	S7
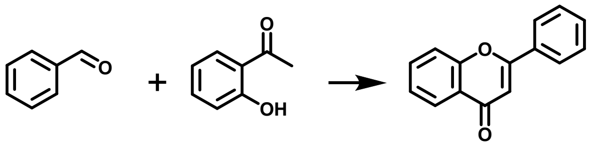 130 °C, open air (1 atm), 24 h.	76	–	S8
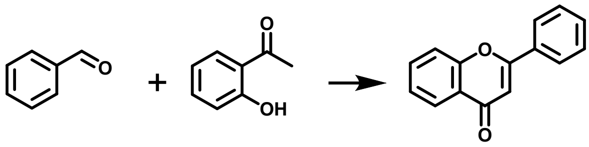 140 °C, 12 h, O_2 (2 bar), *n*-hexanol (4 mL).	99	–	S9
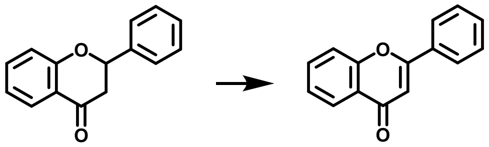 100 °C, 32 h, O_2 (1 bar), HOAc (4 mL).	66	DMSO	S10

Table S8. Summary of flavonoids synthesis by using different catalytic systems.

Heterogeneous catalysts for flavonoids synthesis.				
Substrate	Catalyst	Products	Yield	Ref.
Lignin β-O-4 model compounds	$Fe_3@Ni_1$-ZrO_2	flavone	56.2% (batch reactor)	This wok
Lignin β-O-4 model compounds	$Fe_3@Ni_1$-ZrO_2	flavone	3.3 g g_{cat} h^{-1}	This wok
Lignin β-O-4 model compounds	$Fe_3@Ni_1$-ZrO_2	acacetin	3.8 g g_{cat} h^{-1}	This wok
Benzyl alcohol and 2'-hydroxyacetophenone	CuN_4/CoN_2P_2 @NPC	flavone	99% (batch reactor)	S6
Benzyl alcohol and 2'-hydroxyacetophenone	CoN_3S_1/CuN_4 @NC	flavone	99% (batch reactor)	S7
Benzaldehyde and 2'-hydroxyacetophenone	CuN_4/CoN_4@NC	flavone	99% (batch reactor)	S9
Benzaldehyde and 2'-hydroxyacetophenone	Au/LDH	flavone	76% (batch reactor)	S8
Homogeneous catalysts for flavonoids synthesis.				
Flavanone	$Pd(DMSO)_2(TFA)_2$	flavone	66% (batch reactor)	S10
Biosynthesis of flavonoids and derivatives by systematic engineering of yeast cell				

factories. [a]

Substrate	Engineered yeast	Products	Yield	Ref.
Glucose	S. cerevisiae	Naringenin	2.05 g/L	S12
Glucose	S. cerevisiae	Naringenin	3420.6 mg/L	S13
Glucose	Y. lipolytica	Naringenin	8.3 g/L	S14
Glycerol	P. pastoris	Naringenin	1067 mg/L	S15
Glucose	S. cerevisiae	Eriodictyol	132.1 mg/L	S16
Glucose	Y. lipolytica	Eriodictyol	6.8 g/L	S17
Glucose	S. cerevisiae	Pinocembrin	80 mg/L	S18
Glucose and *p*-coumaric acid	Y. lipolytica	Liquiritigenin	62.4 mg/L	S19
Glucose	S. cerevisiae	Kaempferol, quercetin	956 mg/L, 930 mg/L	S20
Glucose	S. cerevisiae	Taxifolin	336.8 mg/L	S21
Glucose	Y. lipolytica	Taxifolin	110.5 mg/L	S22
Glucose	S. cerevisiae	Genistein	23.31 mg/L	S23
Glucose	S. cerevisiae	Daidzein	85.4 mg/L	S24
Glucose	S. cerevisiae	Delphinidin Pelargonidin Cyanidin	26.1 mg/L 33.3 mg/L 31.7 mg/L	S25
Eriodictyol	S. cerevisiae	Eriocitrin	131.3 mg/L	S26
Glucose	Y. lipolytica	Scutellarin	703.0 mg/L	S27
Glucose	P. pastoris	Baicalin	1290.0 mg/L	S28
Glucose	S. cerevisiae	8-Prenylnaringenin	0.12 mg/L	S29
Glucose	S. cerevisiae	8-Prenylnaringenin	49.4 mg/L	S30

[a] This table was referred to a review (Ref. S11).

References

S1. G. Meng, W. Lan, L. Zhang, S. Wang, T. Zhang, S. Zhang, M. Xu, Y. Wang, J. Zhang, F. Yue, Y. Wu and D. Wang, *J. Am. Chem. Soc.,* 2023, **145**, 12884-12893.

S2. T. Cui, L. Ma, S. Wang, C. Ye, X. Liang, Z. Zhang, G. Meng, L. Zheng, H.-S. Hu, J. Zhang, H. Duan, D. Wang and Y. Li, *J. Am. Chem. Soc.,* 2021, **143**, 9429-9439.

S3. Y. Ding, T. Guo, Z. Li, B. Zhang, F. E. Kühn, C. Liu, J. Zhang, D. Xu, M. Lei, T. Zhang and C. Li, *Angew. Chem. Int. Ed.,* 2022, **61**, e202206284.

S4. P. Li, Y. Ouyang, G. Xiao, Y. Zhao, S. Sarina, J. Baeyens, H. Su and H.-Y. Zhu, *Green Chem.,* 2021, 23, 7780.

S5. B. Zhang, T. Guo, Z. Li, F. E. Kühn, M. Lei, Z. K. Zhao, J. Xiao, J. Zhang, D. Xu, T. Zhang and C. Li, *Nat. Commun.,* 2022, **13**, 3365.

S6. X. Zhao, R. Fang, F. Wang, X. Kong and Y. Li, *JACS Au,* 2023, **3**, 185-194.

S7. X. Zhao, R. Fang, F. Wang and Y. Li, *Small*, 2023, 2304053.

S8. T. Yatabe, X. Jin, K. Yamaguchi and N. Mizuno, *Angew. Chem., Int. Ed.,* 2015, **54**, 13302.

S9. X. Zhao, R. Fang, F. Wang, X. Kong and Y. Li, *Nat. Commun.,* 2022, **13**, 7873.

S10. T. Diao and S. S. Stahl, *J. Am. Chem. Soc.* 2011, **133**, 14566-14569.

S11. J. Wang, C. Chen, Q. Guo, Y. Gu and T.-Q. Shi, *ACS Synth. Biol.,* 2024, **13**, 2667-2683.

S12. S. Gao, H. Zhou, J. Zhou, J. Chen, *J. Agric. Food. Chem.,* 2020, **68**, 6884-6891.

S13. M. Suastegui, W. Guo, X. Feng, Z. Shao, *Biotechnol. Bioeng.,* 2016, **113**, 2676-2685.

S14. M. Liu, J. Wu, M. Yue, Y. Ning, X. Guan, S. Gao, J. Zhou, *Metab. Eng.,* 2024, **82**, 29-40.

S15. R. Kumokita, T. Bamba, K. Inokuma, T. Yoshida, Y. Ito, A. Kondo, T. Hasunuma, *ACS Synth. Biol.,* 2022, **11**, 2098-107.

S16. S. Zhang, J. Liu, Z. Xiao, X. Tan, Y. Wang, Y. Zhao, N. Jiang, Y. Shan, *J. Fungi,* 2024, **10**, 119.

S17. M. Yue, M. Liu, S. Gao, X. Ren, S. Zhou, Y. Rao, J. Zhou, *J. Agric. Food. Chem.,* 2024, **72**, 4292−4300.

S18. M. Tous Mohedano, J. Mao, Y. Chen, *ACS Synth. Biol.,* 2023, **12**, 144-152.

S19. M. Akram, A. Rasool, T. An, X. Feng, C. Li, *Chem. Eng. Sci.,* 2021, **230**, 116177.

S20. M. Tartik, J. Liu, M. T. Mohedano, J. Mao, Y. Chen, *Microb. Cell Fact.,* 2023, **22**, 74.

S21. J. Yang, J. Liang, L. Shao, L. Liu, K. Gao, J. L. Zhang, Z. Sun, W. Xu, P. Lin, R. Yu, J. Zi, *Metab. Eng.,* 2020, **59**, 44-52.

S22. M. Li, C. Liu, J. Yang, R. Nian, M. Xian, F. Li, H. Zhang, *Biotechnol. Adv.,* 2020, **41**, 107548.

S23. Y. Wang, Z. Xiao, S. Zhang, X. Tan, Y. Zhao, J. Liu, N. Jiang, Y. Shan, *J. Fungi,* 2024, **10**, 176.

S24. Y. Du, B. Yang, Z. Yi, L. Hu, M. Li, *J. Agric. Food. Chem.,* 2020, **68**, 2146-2154.

S25. C. Wang, W. Ma, L. Xu, Z. Wei, K. Tang, J. Zhou, *J. Chen, Food Biosci.,* 2024, **60**, 103996.

S26. J. Pei, Q. Sun, L. Zhao, H. Shi, F. Tang, F. Cao, *J. Agric. Food. Chem.,* 2019, **67**, 331−340.

S27. P. Zhang, W. Wei, Y. Shang, B. C. Ye, *Bioresour. Technol.,* 2023, **385**, 129421.

S28. Y. Kang, Z. Qian, H. Yu, J. Lu, Q. Zhao, X. Qiao, M. Ye, X. Zhou, M. Cai, *Small Methods,* 2024, **8**, 2301371.

S29. C. J. Guo, Y. K. Lv, H. B. Li, J. W. Zhou, S. Xu, Syst. *Microbiol. Biomanuf.,* 2023, **3**, 647-658.

S30. K. Zhao, Y. Zhou, C. Qiao, T. Ni, Z. Li, X. Wang, Q. Guo, N. Lu, L. Wei, *J. Hematol. Oncol.,* 2015, **8**, 41.